This is a repository copy of *How to best measure atomic sergregation to grain boundaries by analytical transmission electron microscopy*.

White Rose Research Online URL for this paper:
http://eprints.whiterose.ac.uk/86358/

Version: Accepted Version

Article:

Walther, T., Hopkinson, M., Daneu, N. et al. (4 more authors) (2013) How to best measure atomic sergregation to grain boundaries by analytical transmission electron microscopy. Journal of Materials Science, 49 (11). pp. 3898-3908. ISSN 0022-2461

10.1007/s10853-013-7932-2

Reuse
Unless indicated otherwise, fulltext items are protected by copyright with all rights reserved. The copyright exception in section 29 of the Copyright, Designs and Patents Act 1988 allows the making of a single copy solely for the purpose of non-commercial research or private study within the limits of fair dealing. The publisher or other rights-holder may allow further reproduction and re-use of this version - refer to the White Rose Research Online record for this item. Where records identify the publisher as the copyright holder, users can verify any specific terms of use on the publisher's website.

Takedown
If you consider content in White Rose Research Online to be in breach of UK law, please notify us by emailing eprints@whiterose.ac.uk including the URL of the record and the reason for the withdrawal request.

eprints@whiterose.ac.uk
https://eprints.whiterose.ac.uk/

J Mater Sci
DOI 10.1007/s10853-013-7932-2

INTERFACES AND INTERGRANULAR BOUNDARIES

How to best measure atomic segregation to grain boundaries by analytical transmission electron microscopy

T. Walther · M. Hopkinson · N. Daneu · A. Recnik · Y. Ohno · K. Inoue · I. Yonenaga

Author Proof

Received: 9 July 2013 / Accepted: 28 November 2013
© Springer Science+Business Media New York 2013

Abstract This study provides an overview of the recent experiments employing methods that analyse, systematically, series of analytical spectra acquired either in nanobeam mode in a transmission electron microscope or using elemental mapping in a scanning transmission electron microscope. A general framework is presented that describes how best to analyse series of such spectra to quantify the areal density of atoms contained within a very thin layer of a matrix material, as, for example, appropriate to measure grain boundary segregation. We show that a systematic quantification of spectra as a function of area size illuminated by the electron beam eliminates the large systematic errors inherent in simpler approaches based on spatial difference methods, integration of compositional profiles acquired with highly focused nanoprobes or simple repeats of such measurements. Our method has been successfully applied to study dopant segregation to inversion domain boundaries in ZnO, to quantify the thicknesses of sub-nm thin layers during epitaxial growth by molecular beam epitaxy of (In)GaAs and to prove the absence of gettering of dopants at $\Sigma = 3\{111\}$ grain boundaries in Si, with a precision <1 atom/nm^2 in all these cases.

Introduction

The measurement of elemental segregation to grain boundaries is key to understanding the brittle behaviour of metallic alloys [1] and the anisotropic grain growth in oxide ceramics [2]. This has traditionally been performed by methods that either crack the material in ultrahigh vacuum conditions followed by chemically sensitive surface analysis using Auger electron spectroscopy [3], X-ray photoelectron or secondary ion mass spectroscopy [4], or by methods that prepare a specific grain boundary from within the bulk, which can then be investigated by position-sensitive field-ion microscopy [5] or analytical electron microscopy.

For analysis using an electron microscope, traditionally, profiles across the boundary have been recorded or difference measurements on and off the grain boundary have been compared using scanning transmission electron microscopy (STEM), employing either energy-dispersive X-ray spectroscopy (EDXS) [6] or electron energy-loss spectroscopy (EELS) [7]. Quantification is, in all these cases, limited by a number of factors:

- the statistical spread due to limited counting statistics from analysing volumes that only contain a small number of dopant atoms, leading to statistical error bars of single measurements of typically 0.2–0.6 atoms/nm^2 [8],

Paper presented at IIB 2013 meeting, Athena Pallas Village, Greece, 25 June 2013.

Electronic supplementary material The online version of this article (doi:10.1007/s10853-013-7932-2) contains supplementary material, which is available to authorized users.

T. Walther (✉) · M. Hopkinson
Department of Electronic and Electrical Engineering, University of Sheffield, Mappin Building, Mappin Street, Sheffield S1 3JD, UK
e-mail: t.walther@sheffield.ac.uk

N. Daneu · A. Recnik
Department for Nanostructured Materials, Jožef Stefan Institute, Jamova 39, 1000 Ljubljana, Slovenia

Y. Ohno · K. Inoue · I. Yonenaga
Institute for Materials Research, Tohoku University, Katahira 2-1-1, Aoba-ku, Sendai 980-8577, Japan

Journal : Large 10853 | Dispatch : 10-12-2013 | Pages : 11
Article No. : 7932 | LE | TYPESET
MS Code : JMSC35156 | CP | DISK

UNCORRECTED PROOF

Author Proof

- the knowledge of the sample geometry (specimen thickness and density, and depth of the grain boundary within the sample) and the amount of electron beam spreading associated with this, neglect of which leads to a systematic bias that usually introduces a significant underestimate of the occupancy of a grain boundary by solute atoms, and
- sensitivity of the specimen to electron beam radiation damage, where an attempt to work with a strongly focused electron beam to improve count rates and/or reduce the time of analysis and thereby spatial drift during the experiment can lead to loss of material by knock-on damage, which, if the sputtering thresholds for different atomic species are significantly different, will again introduce systematic errors and so essentially links the two problems mentioned above.

While the limits for detection of impurity segregation to boundaries can be low, e.g. ∼0.1 monolayers (ML) of nitrogen at platelets in diamond [9] or 0.1–1.9 ML of gallium at grain boundaries in aluminium [10], both reproducibility and precision reported are typically worse than the sensitivity, e.g. ∼0.2 ML for bismuth at a tilt grain boundary in copper [11] or 'up to 1 ML of antimony distributed uniformly on the faulted zone' (in zinc oxide) [12]. The precision of 0.1 ML quoted for position-sensitive atom probe field-ion microscopy in [13] corresponds to 2 Ag atoms/nm^2 at an interface between MgO and Cu; in all cases, however, the precision was estimated from statistics rather than compared with known results from a standard specimen.

The recent availability of aberration-corrected electron microscopes has led to a number of publications with stunning images of grain boundary structures at quasi-atomic spatial resolution, mostly recorded in the annular dark-field scanning TEM mode [14], sometimes along two perpendicular zone axes [15]. Also, chemical maps showing atomic-scale details by either EELS [16] or EDXS hyperspectral imaging with multiple solid-state drift (SSD) detectors [17] have recently been presented. While these developments present a breakthrough in atomic structure determination and will be invaluable for developing and testing structural models for grain boundaries, there are a rather large number of physical reasons why chemical quantification of such images and maps has not become easier with improved resolution, but rather more difficult, and to date no such X-ray distribution maps of grain boundary structures have been reliably quantified in terms of atomic numbers per atomic column as far as the authors are aware. The study of grain boundary segregation in a γ/γ' Ni-base superalloy by Watanabe et al. [18] came very close, measuring Zr segregation at ∼1-nm scale resolution; however, the numerical results from the ζ-factor method (2–3 atoms/nm^2) and the scaling of the excess map from principal component analysis (0–0.8 atoms/nm^2) unfortunately did not agree.

- Spherical aberration-corrected STEM with atomic resolution necessitates very thin crystals wherein, by definition, each atomic column consists of only a small number of unit cells (e.g. 20 nm of Si(001) would have 37 Si atoms in each column) so that even the detection of single atomic exchanges would amount to changes of a few at.% (∼3at.% in the above example), and measuring the segregation at the ‰ level would necessitate integration over a rather large number of atomic columns whereby the benefit of in-plane atomic resolution would be somewhat lost;
- the higher noise expected from single atomic exchange statistics in thin samples as explained above can be partially compensated by an improvement of the electron (and, hence, also X-ray) statistics if higher electron probe currents are used; however, these will exacerbate the problem of beam damage by knock-on damage and hole drilling, as exemplified in Fig. 10 in this study;
- the need for zone axis orientations for atomic resolution imaging and spectroscopy makes any analysis highly susceptible to channelling effects [19], and unless the crystal thickness and local orientation are precisely measured and the degree of channelling is modelled by extensive simulations of the probe propagation [20, 21], channelling will make the X-ray production yield depth dependent in a non-linear way and make reliable quantification highly difficult to achieve; and, lastly,
- while atomic resolution imaging and mapping depend on the full width at half maximum (FWHM) of the probe, probe tails mainly due to chromatic aberration and residual aberrations mean that for focused probes the diameters that contain 50 % (d_{50}) or even 90 % (d_{90}) of the total probe intensity will be much larger than the FWHM values and without monochromation can easily be >1 nm [22]. As a result, majority of the signal in an X-ray map that may show an individual atomic column does not actually stem from that specific atomic column alone, but is an integral that extends over several neighbour columns as well, and disentanglement to separate the non-column-specific background may only be achievable by extended multivariate statistical analysis, as recently attempted for a periodic sample in [23].

Similarly, SSD detectors are very useful for standard scanning electron microscopes as they are capable of very high throughputs without saturation [24]; however, the benefit for aberration-corrected STEM with EDXS is again mainly limited to producing atomic-scale maps, if sufficient probe current is available [25, 26], which are difficult to quantify for two reasons:

UNCORRECTED PROOF

Journal : Large 10853 | Dispatch : 10-12-2013 | Pages : 11
Article No. : 7932 | LE | TYPESET
MS Code : JMSC35156 | CP | DISK

161 • the silicon material in SSD detectors is of standard silicon wafer thickness and hence much thinner than in traditional Si:Li or high-purity Ge solid-state detectors, implying that very hard X-rays can be transmitted without detection and the detection efficiency, while improved for soft X-rays if operated window-less [25, 26] will be decreased for hard X-rays; and from discussions with manufacturers, it seems unclear whether the new detector efficiencies have already been measured as reliably as for the previous types of detectors, which has taken them decades;
172 • the benefit of larger detector areas of SSDs compared to standard detectors implies larger collection angles only if these detectors are placed closer to the sample (which in aberration-corrected microscopes with larger pole-piece gaps poses no significant problem); however, in this case, the detectors will integrate over a larger continuous range of take-off angles each of which will need a correspondingly different absorption correction. Only if X-ray absorption is generally so low that it can be neglected all together will the approximation of one discrete take-off angle rather than a range of those remain sufficiently accurate. It may be expected that this could become a major headache for manufacturers and/or operators if they want to quantify X-ray spectra taken under conditions where take-off angles cover a very large angular range that cannot be accurately measured.

188 We have shown that a systematic analysis of a series of spectra instead, taken either from around the grain boundary with varying diameters of the electron beam (in convergent beam nanoprobe mode) [27] or as a function of the width of the raster scan around the grain boundary (in scan mode) [28], based on a linear least-squares fit of the ratio of matrix/solute atoms as a function of beam radius or scan width, yields several advantages over the above-mentioned methods, namely improved reproducibility of the results, higher accuracy and the fact that the accuracy expected can be directly estimated from the regressional coefficients, which is regarded useful for cases where no standards is available for comparison.

201 We have so far done simulations for various conditions [10–13, 27–30] and originally applied the technique using X-ray spectra to measure segregation of antimony (Sb) [31], tin (Sn) [32] and iron (Fe) [33, 34] ions to inversion domain boundaries in doped zinc oxide (ZnO). Then, we have used it to measure the thickness of epitaxial layers only a few monolayers thin of InAs/InP, where the method proved useful to detect an occasionally leaking gas valve [35], and InAs/GaAs [36], where we investigated the onset of islanding (Stranski–Krastanow growth) in strained layer epitaxy. In principle, such ultrathin epitaxial layers can be regarded as artificially created grain boundaries that are sandwiched between the surrounding layers without a change of crystallographic structure and the chemical width of which can be calculated precisely using our approach.

217 It should be noted that our approach measures the integrated signal from atoms or ions segregated to a planar fault very precisely and as such provides a numerical value and an error bar, but it does not have any spatial resolution *per se* and as such will need highly resolved images (and maybe also maps) to develop or test structural models. It can be applied to series of EEL or EDX spectra without complicated multivariate statistical or principal component analysis [28].

226 Here, some of these experiments will be briefly reviewed (doped ZnO studied in nanobeam TEM mode and InGaAs quantum wells investigated by X-ray mapping in STEM), before a new application of the technique to doped grain boundaries in silicon will be presented where the method has been used successfully to rule out segregation of As, and to a less certain degree also of Ga, to a typical $\Sigma = 3\{111\}$ grain boundary in Si.

234 Simulations

235 Simulations of electron beam broadening in a thin foil specimen under kinematic approximations for various image conditions [27, 28] have shown that the apparent concentration of a particular element present in a planar fault or a very thin epitaxial layer imaged edge-one as measured by an electron beam centred above that fault or layer is systematically lower than the value expected from geometrical consideration of the extension of the fault or layer within the area sampled by the incident electron beam. Figure 1 shows typical results from such simulations as appropriate for imaging silicon (Si) with 100 keV electrons. For the smallest beam size considered, of 1 nm radius, a fault 0.2 nm wide and covered by 50 % of solute atoms would cover 6.37 % of the incident area, and this ideal value for a very thin specimen (foil thickness $t \rightarrow 0$) has been used as maximum scale value on the *y*-axis of that figure. For comparison, beam broadening in a specimen of finite thickness *t* would be expected to decrease this value for an incident 2-nm-diameter beam to 6.12 % for $t = 5$ nm, 5.85 % for $t = 10$ nm, 5.15 % for $t = 25$ nm, 3.50 % for $t = 50$ nm, 2.25 % for $t = 100$ nm and 1.32 % for $t = 200$ nm, i.e. for $t > 50$ nm, the apparent concentrations will be less than halved; and even for comparably thin foils of 10–20 nm thickness, the relative underestimate will be 8–19 %. As a consequence, without taking beam broadening into account by explicit modelling, any chemical measurements will yield a significant underestimate of the true solute concentrations. 262

Author Proof
UNCORRECTED PROOF

Journal : Large 10853 Dispatch : 10-12-2013 Pages : 11
Article No. : 7932 LE TYPESET
MS Code : JMSC35156 CP DISK

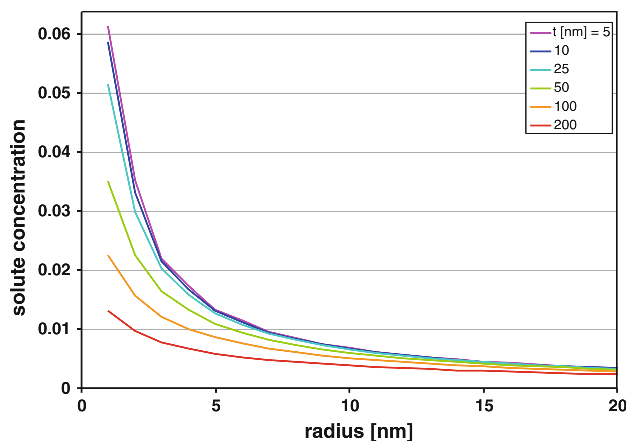

Fig. 1 Simulation of the apparent solute concentration for a planar fault 0.2 nm wide and covered to 50 % by a solute element, for pure Si imaged at 100 kV, X-ray detection from the complete hemisphere above the fault, beam diameters from 2 to 40 nm and specimen thicknesses t as indicated

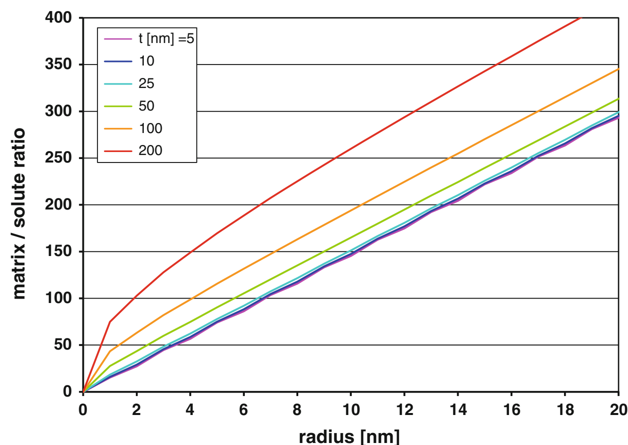

Fig. 2 Simulations as for Fig. 1, but now plotting the inverse, i.e. the matrix/solute ratio as a function of incident beam size

Taking beam broadening into account properly in practice will need an experimental measurement of the specimen thickness, which is difficult to achieve reliably and with sufficient accuracy (thickness fringes are too coarse, convergent beam methods work well only for very large thicknesses and neglect amorphous surface layers, and electron energy-loss spectroscopy relies on the knowledge of either the mean free path or optical properties, both of which will to a certain extent depend on the chemistry which is to be measured and thus only approximately known a priori). If we plot the inverse ratio, as in Fig. 2, of the matrix/solute ratio, we can see that these curves tend to be nearly linear functions of the beam size, which can be understood from the corresponding volumina covered by the fault (a sheet of thickness d, width $2r$ and length t) and the matrix (without beam broadening: a cone of diameter $\sim 2r$ and height t, from which the fault volume needs to be subtracted). Using such a simple geometric approach [27], the intensity ratio of X-ray counts from matrix to solute atoms, corrected for the k-factors of the corresponding lines, has been shown to be given by the following expression, which is thickness independent:

$$R = [(1-x)(\pi r^2 - 2rd)]/[(2rd + \pi r^2 x)] \approx \pi r/(2d) - 1$$

where x is the solid solubility, r is the electron beam radius and d is the effective chemical width of the fault or layer investigated. In the case of a square of width $w = 2r$ scanned in STEM with the fault centred in the middle, the factor π needs to be substituted by the factor 4, yielding an approximate slope of w/d instead of $\pi/(2d)$ [28].

Beam broadening will occur and increase as function of t, thereby introducing non-linearities in the above relationship. Our approach now is based upon measuring several spectra with different beam radii [27] or from scan regions of different widths [28] and using linear regression to determine the slope and its error, which yields the inverse of the effective chemical width of the fault and an error estimate thereof. More details can be found in references [27] and [28].

It should be pointed out that the finite solid solubilities of solute atoms within the matrix will lead to noticeable non-linearities for $x \gg 20$ ppm, as shown in Fig. 3, and the solid solubility itself can be determined reliably either from measurements on such a fault if $x > 1000$ ppm = 1 ‰, as has been done for a thin ilmenite layer with excess iron on (301) twins in rutile mineral [37], or from measurements off the fault. If it is uncertain whether solid solubility will be a potential problem for a given material system, then one can either try to measure the solubility far away from the grain boundary or, if there could be other grain boundaries that are not oriented edge-on and hence

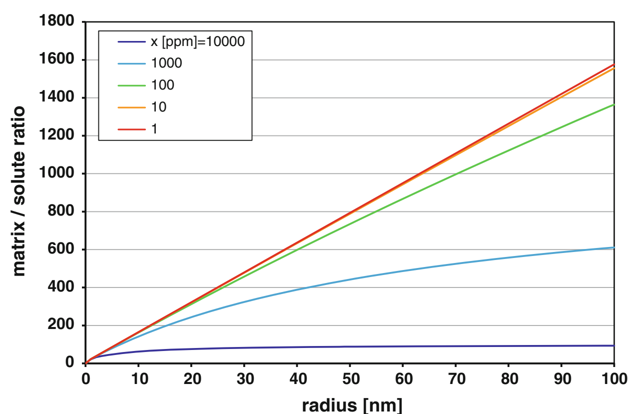

Fig. 3 Simulations as for Fig. 2, but now with a finite solubility, x, of the solute atoms in the matrix. Slight deviations from linearity can be noticed for $x > 20$ ppm [34]

UNCORRECTED PROOF
Author Proof

Journal : Large 10853 Dispatch : 10-12-2013 Pages : 11
Article No. : 7932 □ LE □ TYPESET
MS Code : JMSC35156 ✔ CP ✔ DISK

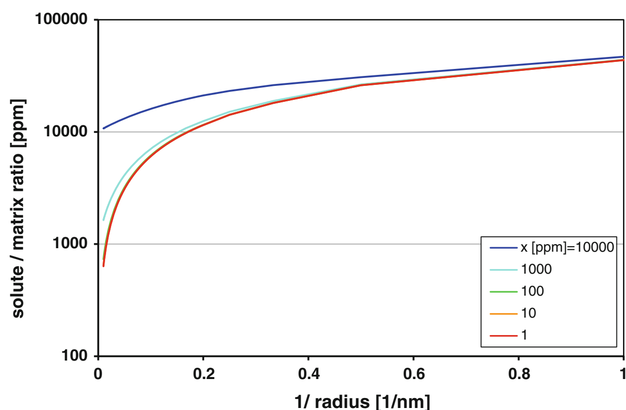

Fig. 4 Simulations as for Fig. 3, but now plotting the measured solute/matrix ratio as function of the inverse beam radius, for different solid solubilities

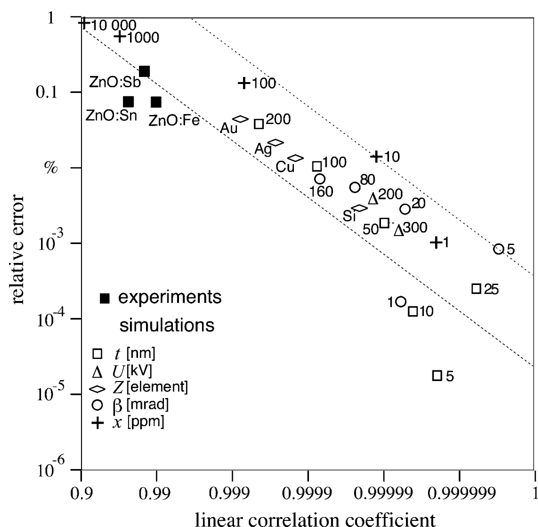

Fig. 5 Comparison of experimental results for three differently doped ZnO samples to numerical simulations (from [34]), showing that precision and linear correlation coefficients are related to each other within a rather narrow corridor marked by *dotted lines*. The simulations for very thin crystals have large error bars because the number of solute atoms within the volume analysed was very small, which introduced sampling artefacts, and the experimental data include additional detector noise from the background subtraction and peak-fitting routines

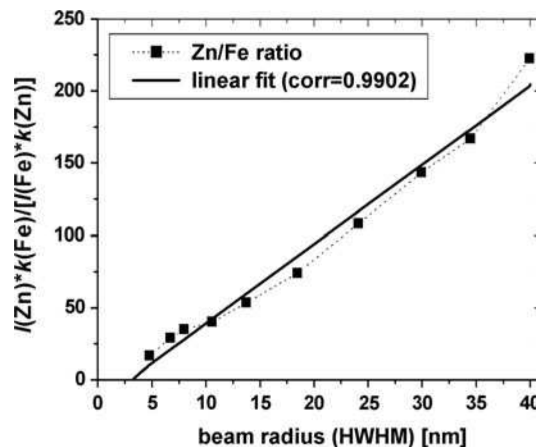

Fig. 6 Result from nanobeam measurements on an inversion domain boundary in Fe_2O_3-doped ZnO (from [38]). The resulting slope converted to 1.02 ± 0.08 of a complete (0002) plane occupied by Fe^{3+} ions

313 not easily visible, plot from the same set of measurements 314 on the one grain boundary under analysis the solute/matrix 315 ratio as function of the inverse beam size. Such a plot is 316 shown in Fig. 4 for the same data as before. The solubility 317 limit can be extracted from extrapolation of a polynomial 318 fit to the curves to the vertical axis, as the limit $1/r \rightarrow 0$ 319 implies $r \rightarrow \infty$, i.e. a situation similar to a bulk study with 320 a defocused electron beam.

321 Figure 5 plots, for all sets of simulations undertaken for 322 the above model with ½ monolayer of segregated dopants, 323 the relative error, i.e. the deviation of the apparent chemical width of the fault from the nominal input value, 324 $\Delta d/d$, as function of the linear correlation coefficient from 325 the linear least-squares fits as described before. The default 326 parameters are $Z = 14$ (Si), $U = 100$ kV, $t = 100$ nm, 327 $x = 0$, $\beta = \pi$, and those single parameters that have been 328 changed have been individually marked. It is clear that 329 almost all data points, with the exception of some referring 330 to very thin silicon, lie within a narrow corridor with a 331 negative slope. This implies that the relative error decreases 332 (and hence, the accuracy improves) as the plots become 333 more linear. In particular, by measuring the linear regression 334 coefficient for any set of measurements, an independent 335 estimate of the expected precision is yielded: for 336 $R^2 = 0.9999$, we would expect a relative deviation of the 337 measured from the correct result by only a few %. 338

$R^2 = 0.99\ldots\ 0.999$ has been achieved in practice, as 339 shown in Fig. 6 for the case of an Fe-doped inversion 340 domain boundary in ZnO, which implies relative errors of a 341 few %, in agreement with further experiments [29–34]. The 342 reasons for the enlarged relative errors are additional statistical 343 variations when performing experiments where 344 individual X-rays are to be counted. 345

Experimental 346

Material growth 347

The ZnO:Fe_2O_3 sample was produced by sintering dry- 348 pressed pellets of polycrystalline ZnO and α-Fe_2O_3 powders 349 in sealed platinum ampoules at a temperature of 350 1350 °C for one day. 351

The InAs/GaAs sample #Vn858 was grown at the 352 National Centre for III/V Technologies of the University of 353

Journal : Large 10853 Dispatch : 10-12-2013 Pages : 11
Article No. : 7932 LE TYPESET
MS Code : JMSC35156 CP DISK

Author Proof
UNCORRECTED PROOF

Author Proof

354 Sheffield by molecular beam epitaxy at nominally 505 °C
355 on n^+-doped GaAs(001) after deposition of buffer layers of
356 1 µm GaAs at 580 °C, 7 µm $Al_{0.35}Ga_{0.65}As$ at 630 °C and
357 another 2 µm GaAs at 580 °C. The InAs quantum wells of
358 nominal thicknesses of 1.6, 1.8 and 2.0 bilayers (mono-
359 layers of the group-III sub-lattice) were separated by
360 nominal 70 nm GaAs so that we could analyse them sep-
361 arately even with larger electron beam sizes.
362 For the latest study, a bulk single crystal of Si, co-doped
363 with Ga and As atoms at concentrations expected from stock
364 weights to be of the order of 10^{-19} cm^{-3}, was grown by the
365 Czochralski method from a melt of As-doped Si and 6 N-
366 grade Ga charged in a silica crucible, with the pulling direc-
367 tion of [001] and a growth rate of 8 mm/h. A thermal shock
368 was applied during growth by rapidly dropping of the growth
369 temperature, which intentionally introduced a single
370 $\Sigma = 3\{111\}$ twin grain boundary that expanded throughout
371 the entire crystal without polycrystallisation. The crystal was
372 then annealed at 900 °C for 100 h so that the dopant atoms
373 could interact with the grain boundary. A small foil with a
374 $(1\bar{1}0)$ surface in which the grain boundary expanded per-
375 pendicular to the surface was cut from the crystal. The loca-
376 tion of the grain boundary was determined by chemical
377 etching with a mixture of $3HNO_3$:1HF at a temperature of
378 300 K, by which the grain boundary was observed as a groove
379 on the surface. Both foil surfaces were mechanochemically
380 polished until the foil was a few µm in thickness. This was
381 then glued onto a molybdenum washer for further handling.

382 Sample preparation

383 Cross-sectional specimens with electron transparent edges
384 were produced by standard methods of mechanical grinding,
385 polishing and argon ion beam milling under angles of typ-
386 ically 7°–10° until perforation. A final polishing step was
387 performed for a few minutes at ion energies of 1–2 keV.

388 Electron microscopy

389 The electron microscopy studies on ZnO were performed
390 using a Philips CM300UT at 300 kV with a Noran high-
391 purity Ge detector for X-rays installed at the University of
392 Bonn, and a JEOL 2010F at 200 kV equipped with an
393 ultrahigh resolution pole piece and an Oxford Instruments
394 Si:Li detector installed at the Josef Stefan Institute in
395 Ljubljana. All experiments on GaAs, InP and Si were
396 performed with a similar JEOL instrument at the Univer-
397 sity of Sheffield. All X-ray detectors had ultrathin polymer
398 windows to shield the cooled semiconductor detectors from
399 the microscope column. For elemental ratios, the measured
400 X-ray counts were corrected by the *k*-factors of the corre-
401 sponding X-ray lines.

Results and discussion 402

Inversion domain boundaries in ZnO doped with Fe, Sn or Sb 403 404

Experiments from three differently doped ZnO samples 405
[29, 31–34] showed that fractional occupancies of mono- 406
layers [in this case, an (0002) plane with octahedral sites in 407
the wurtzite structure] by the solute atoms could be reliably 408
measured, with error bars of 0.4–0.8 atoms/nm^2, in 409
agreement with expectations from simulations [27]. These 410
measurements have been successfully employed to develop 411
a universal model for the formation of such inversion 412
domain boundaries in wurtzite crystal lattices based on the 413
condition of overall charge neutrality which is fulfilled 414
when octahedral interstitial sites that are surrounded by six 415
O^{2-} anions each are filled with cations that are on average 416
trivalent, i.e. the inversion domain boundary consists of a 417
single basal plane which must contain corresponding 418
fractions of Zn^{2+} and ions of different valences (Fe^{3+}, 419
Sn^{4+}, Sb^{5+}) to yield an average charge of 3+. Figure 6 420
shows a typical experimental dataset for ZnO:Fe_2O_3 and its 421
linear regression analysis as explained in the section on 422
simulations. 423

Wetting layer thicknesses in InGaAs/GaAs(001) strained layer epitaxy 424 425

It is well established that InAs/GaAs(001) grows in the 426
Stranski–Krastanow growth mode where the initially flat 427
InAs layer, due to strain, starts islanding if growth con- 428
tinues beyond ~1.8 monolayers (ML) of InAs [39, 40]. 429
This is fundamental for all applications of self-assembled 430
strained quantum dots. The InAs layers grown here were 431
grown by molecular beam epitaxy on GaAs(001) sub- 432
strates at 505 °C to nominal thicknesses of 1.6, 1.8 and 433
2.0 ML, as confirmed by in situ reflection high-energy 434
electron diffraction oscillations, with 70 nm GaAs spacer 435
layers. From X-ray distribution maps acquired with 436
~2 nm/pixel sampling, as shown in Fig. 7, we have 437
extracted the integral counts from the K- and L-lines for 438
each map section around each InAs layer and plotted the 439
As/In ratio, corrected for *k*-factors, as a function of the 440
window length, *L*, perpendicular to each layer (up to a 441
total width of ~110 nm, above which signals from the 442
adjacent layers started to contribute). The resulting plots, 443
shown in Fig. 8, have been subjected to linear regression 444
analysis, and the slopes and their errors extracted and 445
converted to full equivalent (002) monolayers covered by 446
InAs [36]. From the weighted averages of the values 447
extracted for the last flat quantum well (QW2) and the 448
first layer showing quantum dots (QW3), we have cal- 449
culated the onset of the Stranski–Krastanow transition to 450

UNCORRECTED PROOF

Journal : Large 10853 Dispatch : 10-12-2013 Pages : 11
Article No. : 7932 LE TYPESET
MS Code : JMSC35156 CP DISK

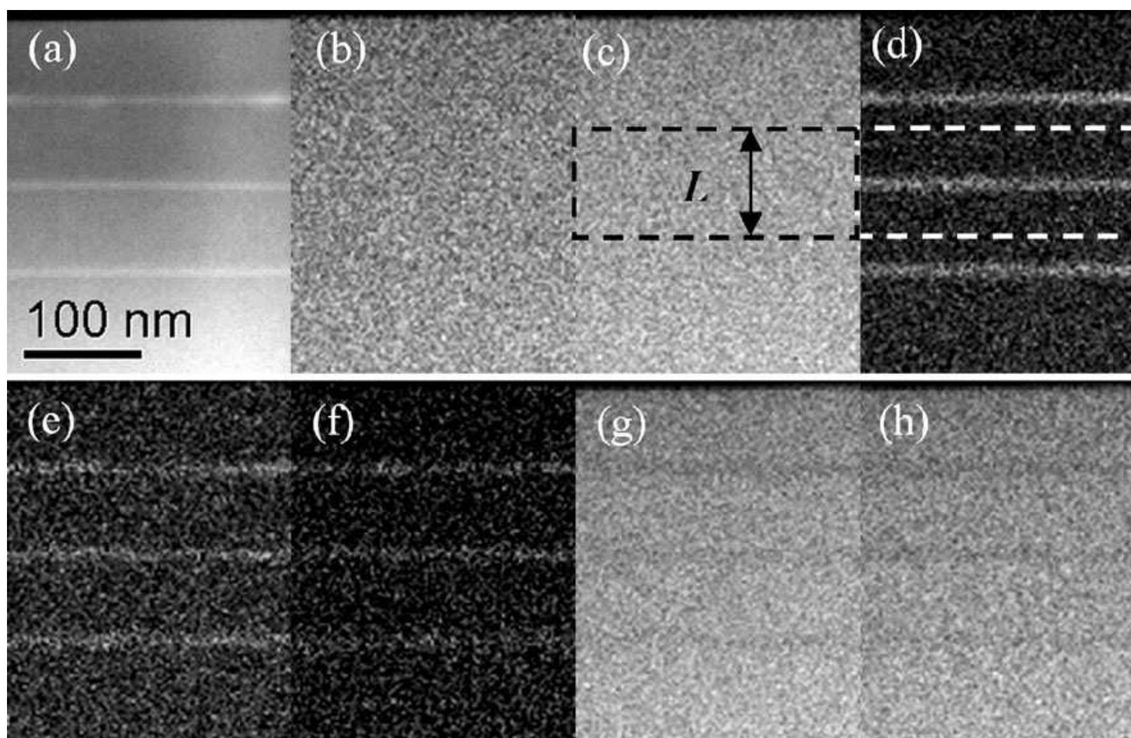

Fig. 7 **a** ADF image and X-ray elemental maps of **b** As_L (30–205 counts), **c** As_K (29–240 counts), **d** $In_{L\alpha}$ (1–33 counts), **e** $In_{L\beta}$ (0–29 counts), **f** $In_{K\alpha}$ (0–20 counts), **g** Ga_L (50–336 counts) and (**h**) Ga_K (32–246 counts) [36]

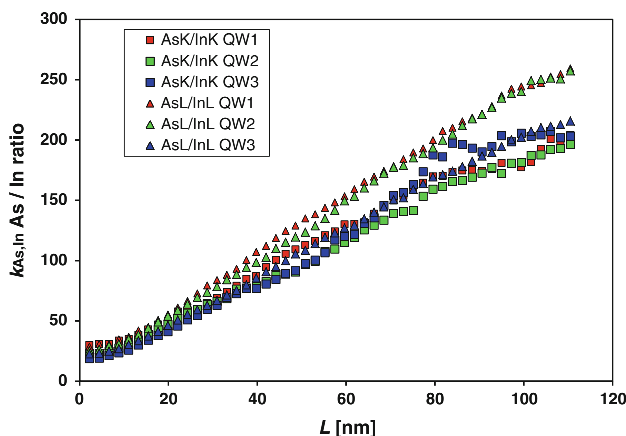

Fig. 8 Plot of *k*-factor-corrected As/In ratio vs window length, *L*, for each of the three quantum wells. The slope is again inversely related to the effective width of the In-containing layers [28, 36] which can thus be calculated. *Squares* are experimental data from K-lines and *triangles* from L-lines

occur around 1.67 ± 0.14 monolayers of InAs, which is in better agreement with references [39, 40] than corresponding values calculated from integration of compositional profiles using either the relative decrease of the Ga signal or the relative increase of the In/(In + Ga) signal [36].

$\Gamma = 3\{111\}$ Si grain boundary doped with Ga and As

The most recent application of our technique has been to $\Gamma = 3\{111\}$ grain boundaries in Si co-doped with Ga and As. A single grain boundary was first located and imaged close to a <110> zone axis. A typical lattice image at 197 kV using the charge-coupled device (CCD) camera behind a Gatan Imaging Filter (GIF 2000) of the JEOL 2010F at the University of Sheffield, recorded at a nominal primary magnification of 50k×, is shown edge-on in Fig. 9. The slight asymmetry of the image pattern on either side of the grain boundary is due to a very small twist component, as confirmed by comparing the precise orientations of the diffraction patterns of the grains from either side of the grain boundary. We found a difference in orientation of 1.3 ± 0.2°, which explains the dark contrast in the lower grain near the left side of the image in Fig. 9. When imaged in scan mode (STEM) with a 9.5 mrad beam convergence (not shown here), bright field imaging revealed the grains with noticeably different contrast, which we attribute to the different crystal orientations, while in high-angle annular dark-field imaging, the grain boundary was sometimes bright, sometimes dark and often invisible, indicating that segregation, if present at all, could not be very strong as Z-contrast could not be observed even for inner collection angles above 55 mrad. If we imaged a

Journal : Large 10853 | Dispatch : 10-12-2013 | Pages : 11
Article No. : 7932 | LE | TYPESET
MS Code : JMSC35156 | CP | DISK

Author Proof

Author Proof

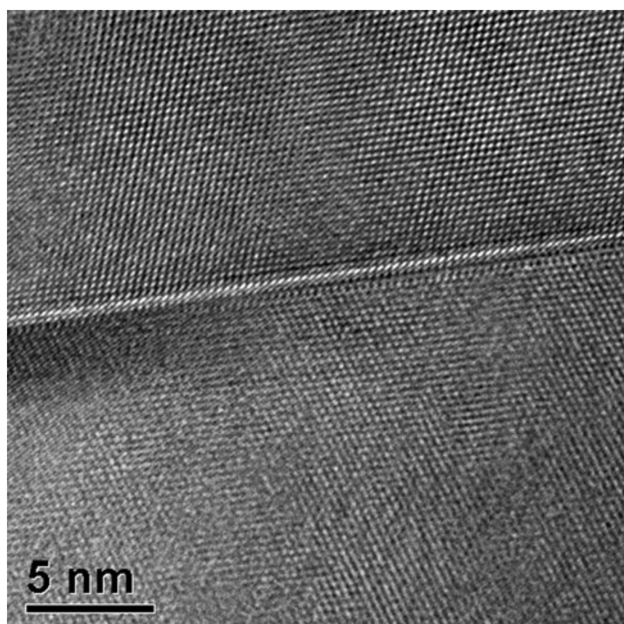

Fig. 9 <110} lattice image of a very thin part of the specimen recorded at ×50 k primary magnification in a JEOL 2010F with Gatan Imaging Filter (GIF 2000), which provides an additional built-in magnification factor of ×~19. The $\Gamma = 3\{111\}$ grain boundary has a small twist component that leads to the asymmetry of the image patterns in both grains

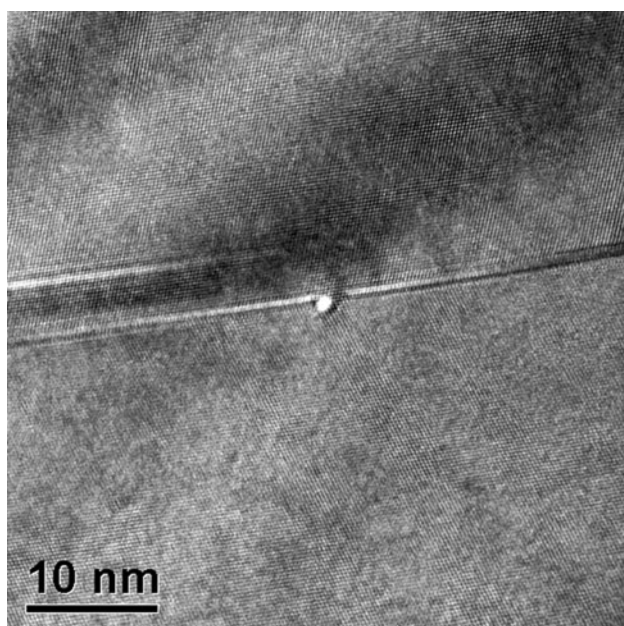

Fig. 10 <110} lattice image of a thicker part of the specimen recorded at ×25k primary magnification in the JEOL 2010F with Gatan Imaging Filter (GIF 2000). The $\Gamma = 3\{111\}$ grain boundary now appears laterally spread due to its inclination in the foil. A spread of ~6 nm for a ~250-nm-thick specimen agrees with the twist component measured by electron diffraction. The 1-nm hole was produced by a focused electron beam of 0.6 nA current in less than 2 s

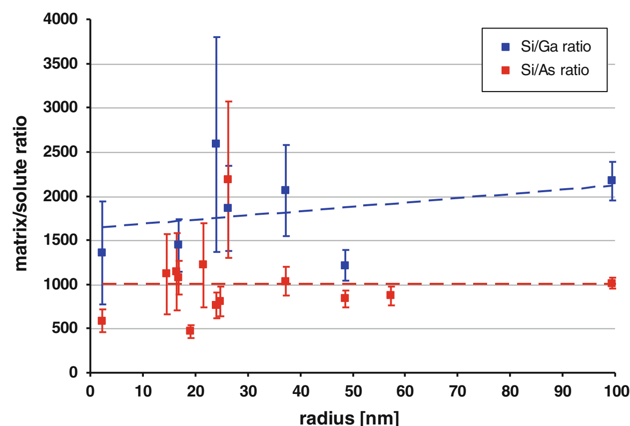

Fig. 11 Plot of Si/Ga (*blue symbols*) and Si/As ratio (*red symbols*) versus electron beam radius measured as full width at half maximum on the CCD camera. Linear fits are marked *dashed*

thicker part of the specimen, we observed that the grain boundary appeared to spread out laterally by several nanometres, which can be directly understood by its inclination with respect to the <110> zone axis orientation. This demonstrates that along this orientation, an investigation by a focused electron beam would have revealed an apparently diffuse interface between the grains. Also, the specimen was so beam sensitive that focusing the ~0.6nA intense beam drilled a hole into the specimen within less than 2 s, during which no useful chemical analysis by energy-dispersive X-ray spectroscopy (EDXS) could have been preformed. In order to avoid quantification problems due to diffraction effects and hole drilling, we tilted the specimen a few degrees further towards the X-ray detector and generally worked with a beam wider than 20 nm (only two spectra with ~4.5 nm probe diameter were recorded, which already indicated some surface etching), and successive spectra were acquired from regions laterally displaced far enough that in the images of the beam profiles recorded with the grain boundary almost edge-on in the middle of the electron beam no further loss of material was apparent (Fig. 10).

We then recorded almost 20 X-ray spectra with different sizes of the electron beam and quantified the chemical composition of all spectra using Oxford Instrument's ISIS 300 software (revision 3.2), taking into account nominal *k*-factors and all lines detected which, apart from >90at.% Si_K, included a few at.% O_K from surface oxidation and similar amounts of $Mo_{K\alpha,\beta}$ from the metal grid supporting the specimen, as well as ≪1at.% from Fe_K (stray signal from steel near the pole piece) and Ga_K and As_K from the doping. Spectra where the Ga and As signals were below the standard errors from counting statistics and background subtraction were discarded from further analysis; for those with signals above the detection threshold of ~0.03at.%,

Journal : Large 10853 Dispatch : 10-12-2013 Pages : 11
Article No. : 7932 ☐ LE ☐ TYPESET
MS Code : JMSC35156 ☑ CP ☑ DISK

Author Proof

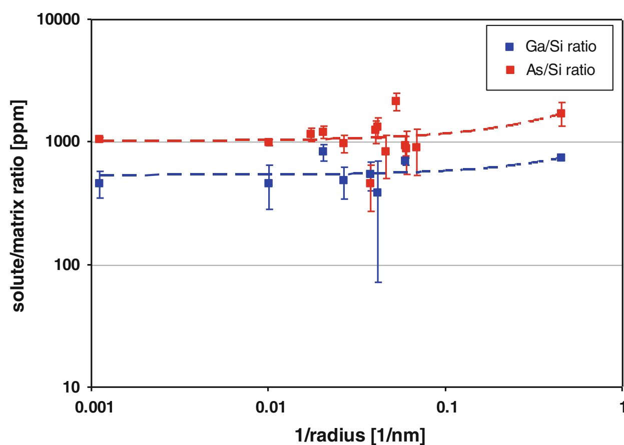

Fig. 12 plot of Ga/Si (*blue symbols*) and As/Si ratio (*red symbols*) vs inverse of the electron beam radius on a double-log scale. Note that linear *fits* appear curved on this scale

Table 1 Numerical analysis of plots from Figs. 11 and 12 for $\Sigma = 3\{111\}$ Si grain boundary

Solute X-ray line	Ga K	As K
x_{solute} (ppm) from all X-ray spectra with K-line intensity > standard error	520 ± 130	1170 ± 310
x_{solute} (ppm) from inverse of y-offset of matrix/solute vs r plots in Fig. 11	610 ± 117	1006 ± 200
x_{solute} (ppm) from y-offset of solute/matrix vs $1/r$ plots in Fig. 12	536 ± 62	1024 ± 121
R^2 of linear fit to matrix/solute ratio vs r in Fig. 11	0.0909	0.0009
Slope of linear fit of matrix/solute ratio vs r (nm^{-1}) in Fig. 11	4.78 ± 6.77	–0.05 ± 0.49
y-offset in multiples of error bars for linear fits to matrix/solute ratio vs r in Fig. 11	5.21	5.03

the ratio of Si/Ga (and Si/As) has been plotted as function of beam radius in Fig. 11.

The plot of Si/solute ratio vs electron beam radius in Fig. 11 and the double-log plot of the inverse ratios versus inverse of the electron beam radius in Fig. 12 were all subjected to standard linear regressional analysis, the numerical results of which are listed in Table 1. It is clear that the Si/As ratio is fairly constant, with a regression coefficient close to zero, indicating the absence of any As segregation. A solid solubility of $\sim$1000 ppm = 1 ‰ is obtained for As, and as suggested previously [27] this can be measured most reliably from extrapolating the plot in Fig. 12 (where the limit $1/r \rightarrow 0$ means $r \rightarrow \infty$ so that the measurements should not be influenced by the grain boundary present any more at all). For Ga, there is a slight positive linear trend in the dataset of Fig. 11, with a correlation coefficient of 0.0909; however, due to the lower overall concentration of this element, only data points from seven spectra could be included in Fig. 11 and eight data points in Fig. 12. These indicate a solid solubility of Ga of $\sim$530 ppm, which almost approaches the detection threshold for transition metals of $\sim$0.03at.% and shows that we are pushing the limits of the technique. If we calculate the ratios of the measured solubilities from the y-offsets of the fits in Fig. 11 to the corresponding error bars in the matrix/solid ratio, we get ratios of $\sim$5 for both elements, indicating that we can exclude segregation to the grain boundary within 5σ intervals which, if the statistics were binomial, would correspond to a confidence interval well over 99 %.

Grain boundary segregation in the presence of a solid solubility of $\sim$1000 ppm = 10^{-3} should have produced strongly bent curves through the origin, as simulated in Fig. 3, which would be very difficult to reconcile with the data measured in Fig. 11.

Our finding is in agreement with the literature data which indicate that $\Gamma = 3$ grain boundaries in silicon have rather compact dislocation cores, do not lead to significant grain boundary grooving during growth from the melt [41], are usually electrically inactive [42] and neither exhibit segregation of transition metal cations [43] nor oxygen [44], although segregation of both carbon [45] and silicon vacancies [46] have been reported. This implies that co-segregation of gallium and arsenic at similar levels could have occurred as long as charge neutrality had been retained. We can, however, exclude this from the above measurements.

Conclusions

With the methodology proposed, it is possible to measure grain boundary segregation with a precision and accuracy down to $\sim$0.1 at/nm^2 in theory, while we typically obtained error bars of $\sim$0.4at/nm^2 in our experiments for doped inversion domain boundaries in ZnO. This has been sufficient to distinguish fractional coverage of a single octahedral monolayer by $^1/_3$, ½ and a complete monolayer and thus paved the way to a general model for cation segregation to inversion domain boundaries in wurtzite lattices.

The method has also been applied to determine the thicknesses of thin InAs wetting layers in strained epitaxial growth of InGaAs to $\sim$0.1 monolayer precision, in good agreement with other methods, and the uncertainty of 1.67 ± 0.14 ML of InAs for the onset of the Stranski–Krastanow transition has been mainly due to the need to study one layer just below and one just above the islanding transition.

UNCORRECTED PROOF

Journal : Large 10853 | Dispatch : 10-12-2013 | Pages : 11
Article No. : 7932 | ☐ LE | ☐ TYPESET
MS Code : JMSC35156 | ☑ CP | ☑ DISK

In the case of a Ga and As co-doped $\Sigma = 3\{111\}$ grain boundary in Si, we could measure the doping levels as $n_{Ga} = 5 \times 10^{-4}$ (500 ppm) and $n_{As} = 1 \times 10^{-3}$ (1000 ppm) and rule out any As segregation. The Ga concentration was just above the detection limit and thus the counting statistics too low to measure reliably any segregation to the grain boundary; however, modelling indicates that the segregation levels cannot be significant for Ga either.

References

1. Viswanathan R (1971) Temper embrittlement in a Ni–Cr steel containing phosphorus as impurity. Metall Trans 2(3):809–816
2. Daneu N, Recnik A, Bernik S, Kolar D (2000) Microstructural development in SnO_2-doped ZnO–Bi_2O_3 ceramics. J Am Ceram Soc 83(12):3165–3171
3. Harris LA (1968) Some observations of surface segregation by Auger electron emission. J Appl Phys 39(3):1428–1431
4. Benninghoven A (1970) Analysis of monomolecular layers of solids by secondary ion emission. Z Phys 230(5):403–417
5. Cerezo A, Godfrey TJ, Smith GDW (1988) Application of a position-sensitive detector to atom probe microanalysis. Rev Sci Instr 59:862–866
6. Bender B, Williams DB, Notis MR (1980) Investigation of grain boundary segregation in ceramic oxides by analytical scanning-transmission electron-microscopy. J Am Ceram Soc 63(9–10): 542–546
7. Müllejans H, Bruley J (1994) Improvements in detection sensitivity by spatial difference electron-energy-loss spectroscopy at interfaces in ceramics. Ultramicroscopy 53(4):351–360
8. Müllejans H (2003) Quantification of interfacial segregation by analytical electron microscopy. Z Metallkunde 94(3):298–306
9. Bruley J (1992) Detection of nitrogen at (100) platelets in a type IAA/B diamond. Philos Mag Lett 66(1):47–56
10. Schmidt S, Sigle W, Gust W, Rühle M (2002) Gallium segregation at grain boundaries in aluminium. Z Metallkd 93(5): 428–431
11. Alber U, Müllejans H, Rühle M (1997) Improved quantification of grain boundary segregation by EDS in a dedicated STEM. Ultramicroscopy 69(2):105–116
12. Bruley J, Bremer U, Krasevec V (1992) Chemistry of basal-lane defects in zinc oxide -antimony oxide (0.1 mol%) ceramics. J Am Ceram Soc 75(11):3127–3128
13. Shashkov DA, Muller DA, Seidman DN (1999) Atomic-scale structure and chemistry of ceramic/metal interfaces-II. Solute segregation at MgO/Cu (Ag) and CdO/Ag (Au) interfaces. Acta Mater 47(15–16):3953–3963
14. Shibata N, Pennycook SJ, Gosnell TR, Painter GS, Shelton WA, Becher PF (2004) Observation of rare-earth segregation in silicon nitride ceramics at subnanometre dimensions. Nature 428(6984): 730–733
15. Winkelman GB, Dwyer C, Hudson TS, Nguyen-Manh D, Döblinger M, Satet RL, Hoffmann MJ, Cockayne DJH (2005) Three-dimensional organization of rare-earth atoms at grain boundaries in silicon nitride. Appl Phys Lett 87(6):061911
16. Muller DA, Fitting Kourkoutis L, Murfitt M, Song JH, Hwang HY, Silcox J, Dellby N, Krivanek OL (2008) Atomic-scale chemical imaging of composition and bonding by aberration-corrected microscopy. Science 319:1073–1076
17. von Harrach HS, Dona P, Freitag B, Soltau H, Niculae A and Rohde M (2010) An integrated multiple silicon drift detector system for transmission electron microscopes, Proc. EMAG-2009, Sheffield, J Phys Conf Ser 241, 012015
18. Watanabe M, Ackland DW, Burrows A, Kiely CJ, Williams DB, Krivanek OL, Dellby N, Murfitt MF, Szilagyi Z (2006) Improvements in the X-ray analytical capabilities of a scanning transmission electron microscope by spherical-aberration correction. Microsc Microanal 12(6):515–526
19. Tafto J, Spence JCH (1982) Atomic site determination using the channeling effect in electron-induced X-ray emission. Ultramicroscopy 9(3):243–247
20. Allen LJ, Josefsson TW, Rossouw CJ (1994) Interaction delocalization in characteristic X-ray emission from light elements. Ultramicroscopy 55:63–70
21. Rossouw CJ, Forwood CT, Gibson MA, Miller PR (1997) Generation and absorption of characteristic X-rays under dynamical electron diffraction conditions. Micron 28(2):125–137
22. Walther T, Stegmann H (2006) Preliminary results from the first monochromated and aberration corrected 200 kV field-emission scanning transmission electron microscope. Microsc Microanal 12(6):498–505
23. Kotula PG, Klenov DO, von Harrach HS (2012) Challenges to quantitative multivariate statistical analysis of atomic-resolution X-ray spectra. Microsc Microanal 18(4):691–698
24. Leutenegger P, Kemmer J, Lechner P, Soltau H, Weber U, Strüder L, Longoni A, Fiorini C (2000) Silicon drift detectors as radiation monitor for X-, gamma rays and particles. Proc SPIE 4012:579–591 (eds Trumper JE and Aschenbach B)
25. Falke M, Mogilatenko A, Kirmse H, Neumann W, Brombacher C, Albrecht M, Bleloch A, Tränkle G, Käppel A, Terborg R, Kroemer R, Rohde M (2009) XEDS with SDD technology in scanning transmission electron microscopy. Microsc Microanal 15(S2):202–203
26. von Harrach HS, Dona P, Freitag B, Soltau H, Niculae A, Rohde M (2009) An integrated silicon drift detector system for FEI Schottky field emission transmission electron microscopes. Microsc Microanal 15(S2):208–209
27. Walther T (2004) Development of a new analytical electron microscopy technique to quantify the chemistry of planar defects and to measure accurately solute segregation to grain boundaries. J Microsc 215(2):191–202
28. Walther T (2006) Linear least-squares fit evaluation of series of analytical spectra from planar defects: extension and possible implementations in scanning transmission electron microscopy. J Microsc 223(2):165–170
29. Walther T, Daneu N, Recnik A (2004) A new method to measure small amounts of solute atoms on planar defects and application to inversion domain boundaries in doped zinc oxide. Interface Sci 12:267–275
30. Walther T (2008) A comparison of transmission electron microscopy methods to measure wetting layer thicknesses to sub-monolayer precision, Proc. EMAG 2007, Glasgow, J Phys Conf Ser 126, 012091
31. Recnik A, Daneu N, Walther T, Mader W (2001) Structure and chemistry of basal-plane inversion boundaries in Sb_2O_3-doped zinc oxide. J Am Ceram Soc 84(11):2657–2668
32. Daneu N, Recnik A, Walther T, Mader W (2003) Atomic structure of basal-plane inversion boundaries in SnO_2-doped ZnO. Microsc Microanal 9(S3):286–287
33. Walther T, Recnik A and Daneu N (2005) ConceptEM: a new method to quantify solute segregation to interfaces or planar defect structures by analytical TEM and applications to inversion domain boundaries in doped zinc oxide, Proc. Microscopy of Semiconducting Materials (MSM-14), Oxford, UK, Springer Proceedings in Physics 107, 199–202
34. Walther T, Recnik A, Daneu N (2006) A novel method of analytical transmission electron microscopy for measuring highly

Journal : Large 10853 | Dispatch : 10-12-2013 | Pages : 11
Article No. : 7932 | LE | TYPESET
MS Code : JMSC35156 | CP | DISK

Author Proof
UNCORRECTED PROOF

accurately segregation to special grain boundaries and planar defects. Microchim Acta 155:313–318

35. Walther T (2007) Determining buried wetting layer thicknesses to sub-monolayer precision by linear regression analysis of series of spectra, Proc. Microscopy of Semiconducting Materials (MSM-15), Cambridge, Springer Proc Phys 120, 247–250
36. Walther T and Hopkinson M (2010) Quantitative investigation of the onset of islanding in strained layer epitaxy of InAs/GaAs by X-ray mapping in STEM, Proc. Microscopy of Semiconducting Materials (MSM-16), Oxford, J Phys Conf Ser. 209, 012035
37. Daneu N, Schmid H, Recnik A, Mader W (2007) Atomic structure and formation mechanism of 301 rutile twins from Diamantina (Brazil). Am Mineralogist 92(11–12):1789–1799
38. Walther T, Wolf F, Recnik A, Mader W (2006) Quantitative microstructural and spectroscopic investigation of inversion domain boundaries in zinc oxide ceramics sintered with iron oxide. Int J Mat Res 97(7):934–942
39. Leonard D, Pond K, Petroff PM (1994) Critical layer thickness for self-assembled InAs islands on GaAs. Phys Rev B 50(16): 11687–11692
40. Nabetani Y, Yamamoto N, Tokuda T, Sasaki A (1995) Island formation of InAs grown on GaAs. J Cryst Growth 146(1–4): 363–367
41. Fujiwara K, Ishii M, Maeda K, Koizumi H, Nozawa J, Uda S (2013) The effect of grain boundary characteristics on the morphology of the crystal/melt interface of multicrystalline silicon. Scripta Mater 69(3):266–269
42. Matsuki N, Ishihara R, Baiano A, Hiroshima Y, Inoue S, Beenakker CIM (2008) Characterization of local electrical property of coincidence site lattice boundary in location-controlled silicon islands by scanning probe microscopy. Mat Res Soc Symp Proc 1025:B16
43. Suvitha A, Venkataramanan NS, Sahara R, Mizuseki H, Kawazoe Y (2010) First-principles calculations on Sigma 3 grain boundary transition metal impurities in multicrystalline silicon. Jpn J Appl Phys 49:4 04DP02
44. Tsurekawa S, Seguchi T, Yoshinaga H (1994) Grain boundary structure and segregation in direct-bonded silicon bicrystal. Mater Trans, JIM 35(11):777–781
45. Kuchiwaki I, Sugio K, Yanagisawa O, Fukushima H (2008) EELS analysis of 111 Sigma 3 and 112 Sigma 3 twin boundaries and their junctions in phosphor-doped cast polycrystalline silicon. Sol Energy Mater Sol Cells 92:71–75
46. Feng CB, Nie JL, Zu XT, Al-Jassim MM, Yan YF (2009) Structure and effects of vacancies in Sigma 3{112} grain boundaries in Si. J Appl Phys 106(11):113506

Author Proof

UNCORRECTED PROOF

Journal : Large 10853 Dispatch : 10-12-2013 Pages : 11
Article No. : 7932 LE TYPESET
MS Code : JMSC35156 CP DISK